Journal of Power Sources 247 (2014) 991–998

Contents lists available at ScienceDirect

Journal of Power Sources

journal homepage: www.elsevier.com/locate/jpowsour

Improved anode materials for lithium-ion batteries comprise non-covalently bonded graphene and silicon nanoparticles

Yun-Sheng Ye [a,b], Xiao-Lin Xie [c], John Rick [a], Feng-Chih Chang [b,*], Bing-Joe Hwang [a,*]

[a] Department of Chemical Engineering, National Taiwan University of Science and Technology, Taipei, Taiwan
[b] Department of Materials and Optoelectronic Science, Nation Sun Yat-Sen University, Kaohsiung, Taiwan
[c] School of Chemistry and Chemical Engineering, Huazhong University of Science & Technology, Wuhan, China

HIGHLIGHTS

- Si/graphene composites obtained by a self-assembly technique.
- Si nanoparticles are homogeneously distributed on the graphene sheets.
- A significant enhancement of the cycling stability for the Si/graphene composite.
- A capacity of 803 mAh g^{-1} in 100 cycles and <0.25% capacity decreasing per cycle before 150 cycles.

GRAPHICAL ABSTRACT

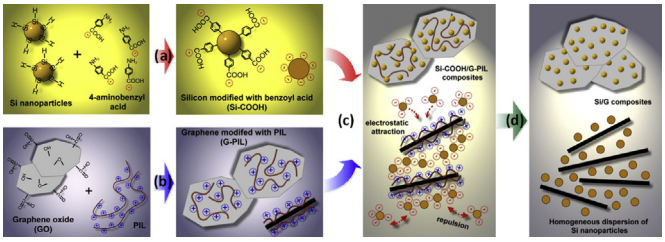

ARTICLE INFO

Article history:
Received 17 June 2013
Received in revised form
31 July 2013
Accepted 14 August 2013
Available online 27 August 2013

Keywords:
Anode materials
Lithium-ion battery
Non-covalently bonded
Graphene

ABSTRACT

Si, when compared to conventional graphite, offers an order-of-magnitude improvement as a high capacity anode material for Li-ion batteries. Despite significant advances in nanostructured Si-based anodes, the formation of stable Si anodes remains a challenge, due to the significant volume changes that occur during lithiation and delithiation. Si/graphene composites, with graphene sheets and Si nanoparticles bound in a dispersion obtained by a self-assembly technique using non-covalent electrostatic attraction (following thermal processing to remove residual organic material) are used to prepare Si-based anodes for use in Li-ion batteries. A mesoporous structure, obtained by further thermal processing is able to accommodate large Si nanoparticle volume changes during cycling, thereby facilitating Li-ion diffusion within the electrode. Morphological analysis showed that Si nanoparticles are homogeneously distributed on the graphene sheets, which is thought to account for the excellent electrochemical performance of the resulting Si/graphene composite. A composite containing Si 67.3 wt% exhibits a greatly improved capacity and cycling stability in comparison with bare Si in combination with the thermal reduction of a simple mixture of graphene oxide and Si nanoparticles without electrostatic attraction (Si content = 64.6 wt%; capacity of 512 mAh g^{-1} in 40th cycle).

1. Introduction

To meet the demands imposed by the rapid development of portable electric devices and electrical vehicles, new anode materials with high capacities and long cycle performances for Li-ion batteries are being sought [1,2]. Among the potential anodic materials, Si is currently the most promising, owing to its high natural abundance, low discharge potential, and high theoretical charge capacity (i.e., 4200 mAh g^{-1}), which is ten times higher than that of graphite (372 mAh g^{-1}) [3–6]. However, there are huge volume changes (up to 270% for the $Li_{3.75}Si$ phase) with consequent Si electrode isolation, during lithiation and delithiation, that can lead to the degradation of Si

* Corresponding authors.
E-mail address: changfc@mail.nctu.edu.tw (F.-C. Chang).

0378-7753/$ – see front matter
http://dx.doi.org/10.1016/j.jpowsour.2013.08.048

nanoparticles and rapid capacity fading [7–9]. Tremendous efforts have been made to overcome these issues and improve the overall electrochemical performance of Si anodes by: decreasing Si particle sizes [4,10], dispersing the Si particles into a conducting matrix [11,12], and using special binders or conductive additives [13,14]. Using carbonaceous materials, such as amorphous carbon [15], carbon nanotubes [16,17], carbon nanofibers [18,19], graphite [20] not only restricts the large volume changes in Si, thereby helping to maintain electrode integrity, but also enhances electrical conductivity.

Graphene, which comprises a one-atom-thick two-dimensional honeycomb carbon lattice, has attracted increasing attention in recent years, mainly due to its: superior thermal and electrical conductivity, excellent mechanical properties, large specific surface area, and low cost [21–23]. The use of graphene has been explored for various applications such as: electronic and energy storage devices [24,25], sensors [26,27], transparent electrodes [28], and composites [29–31]. The combination of their extraordinary inherent physical properties, combined with their ability to be used as a conducting and buffering matrix in Si anodes has led to improvements in reversible capacity, cyclability and the rate capability of Li-ion batteries' electrodes [32]. However, Si nanoparticles are difficult to homogeneously disperse within graphene layers by simple mechanical blending [32,33], or by filtration-directed assembly approaches [34,35], which usually result in the kinetic fading of the electrodes, due to the aggregation of the Si nanoparticles and stacking of the graphene sheets. This problem is a key issue that needs to be addressed in order for a composite to exhibit a good performance.

In order to maintain good structural stability and electron conduction during charging and discharging, the design of the Si nanoparticles/graphene composite needs to be considered. Recently, the covalent anchoring of Si nanoparticles onto the surface of carbon materials (graphite, carbon nanotube and graphene) has proved to be an effective method to prevent the aggregation of the Si nanoparticles and stacking of the carbon materials. These approaches have succeeded in improving the electronic conduction and structural stability of a Si negative electrode for lithium ion batteries. Strong interaction between the Si nanoparticles and graphene sheets in Si/graphene (Si/G) composite is a key issue to the development of anode material with high electrochemical performance for lithium batteries. However, the self-linkage of Si nanoparticles and graphene sheets is difficult to avoid making it difficult to control the graphene sheet to Si nanoparticle grafting ratio. Non-covalent bonding offers several novel strategies for materials design, because non-covalent bonding is inherently reversible, highly tunable, avoids potential side reactions, and provides unlimited processability [36]. In this study, a novel Si/G composite was fabricated by non-covalent anchoring of Si nanoparticles onto the surface of graphene sheets by electrostatic attraction followed by thermal processing to generate nanospaces surrounding the Si nanoparticles, thereby forming a mesoporous structure (Fig. 1). The presence of non-covalent linkages prevents the aggregation of Si nanoparticles and guarantees their uniform insertion into the graphene layers without any Si nanoparticle to Si nanoparticle, or graphene nanosheet to graphene nanosheet self-linkage (due to the negative charges on the Si nanoparticles and the positive charges on the graphene nanosheets guaranteeing mutual repulsion). In addition, the mesoporous structure of the Si/G composite allows for the free expansion and contraction of Si nanoparticles, during lithiation and delithiation, without mechanical constraint or tension. To complete fabrication of Si/G composite includes two points: (1) the Si nanoparticles and graphene sheets modified with opposite surface charge to allow the formation non-covalent bond through electrostatic attraction; and, (2) the organic materials (including polymer) surrounding Si nanoparticle leave sufficient empty space after thermal process providing an elastic buffer to accommodate the volume variation of Si nanoparticles during Li alloying and dealloying processes. The resulting Si/G (Si/G 3/1) composite delivers a reversible capacity of 803 mAh g^{-1} in the 100th cycle and a high capacity retention (>75%) before 100 cycles with a high rate capability. These important issues are highlighted by comparing the composite electrodes' performance to that found with a thermally reduced mixture simply comprising graphene oxide (GO) and Si nanoparticles without any electrostatic attraction [Si/reduced grapheme oxide (RGO)]. We believe this technique can be applied to other carbon conductive additives together with Si or other nanosized active compounds.

2. Experimental section

2.1. Preparation of negatively charged Si (Si–COOH) and positive charged graphene [graphene-modified protic ionic liquid (G-PIL)]

Si nanoparticles were pre-treated with a HF (4%) solution under a nitrogen atmosphere for hydrogen passivation in accordance with

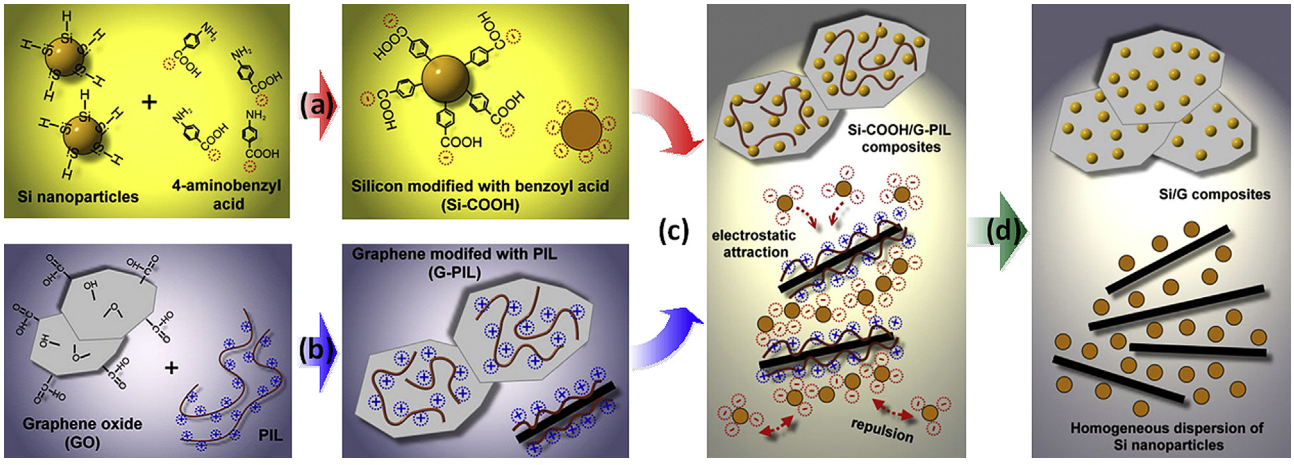

Fig. 1. Fabrication of Si/G composites: (a) negatively charged Si nanoparticles, modified with 4-aminobenzyl acid, (b) positively charged graphene nanosheets, modified with PIL, (c) Self-assembly between Si–COOH and G-PIL mediated by electrostatic attraction, (d) Thermal processes leave empty spaces between the Si nanoparticles and the graphene nanosheets.

a previously published study [5,16]. Si nanoparticles (50 mg) and amino benzoyl acid (1 g) were dispersed in CH_3CN (20 mL) by ultrasonication, then iso-amyl nitrite (5 mmol) was added to the mixture with stirring. After reaction for 4 h at ambient temperature, the mixture was filtered, and then successively washed with water and ethanol. The resulting powder was dried under vacuum at ambient temperature overnight. The preparation of G-PIL by reduction of graphene and PIL mixing solution was similar to that reported in our previous study [30].

2.2. Preparation of Si/G and Si/RGO composites

The Si–COOH and G-PIL were separately dispersed in water (concentration of 1 mg mL^{-1}) by sonication. Then, the Si–COOH/G-PIL composites with different components of Si–COOH and G-PIL (Si–COOH/G-PIL = 3/1, 2/1, 1/1, 1/2; Table 1) were prepared by slowly introducing the G-PIL dispersion into the Si–COOH dispersion to make the positively charged uniformly assemble of G-PIL coalesce with the negatively charged Si–COOH through electrostatic attraction. The aqueous dispersion was freeze-dried and following thermal processing at 500 °C, for 1 h, under a nitrogen atmosphere, Si/G composites were obtained. A control sample of Si/RGO composite was prepared using a similar procedure by replacing Si–COOH with pristine Si nanoparticles and G-PIL with GO (weight ratio of Si to GO = 3:2).

2.3. TGA analysis and theoretical calculations

Thermogravimetric analyses (TGA) were undertaken using a Q50 instrument. The temperature scan was ramped between 50 and 700 °C, at a rate of 10 °C min^{-1}, under nitrogen for Si–COOH, G-PIL, PIL and the Si–COOH/G-PIL composite (Fig. S1): and under air for Si/RGO and all Si/G composites, Fig. S2. The weight percentage of Si present in the Si/G composites was calculated by the following equation:

$$W_C = W_{Si} \times W_G + W_G \times (1 - X_{Si}) \quad (1)$$

Where: W_{Si}, W_G and the W_C are the residual weight percentages of Si (W_{Si} = 108.8 wt%), G (graphene from G-PIL; G = 16.8 wt%) and the Si/G composite at 700 °C and X_{Si} is the content of Si in the Si/G composite (graphene from GO; G = 8.4 wt% for calculation of Si content in Si/RGO composite).

2.4. Electrochemical measurements

The preparation of the Si/G and Si/RGO electrodes was carried out by mixing Si/G (or Si/RGO) powder, carbon black and sodium carboxymethyl cellulose (CMC) at a weight ratio of 5:3:2 in deionized water, as the solvent, to form a homogeneous slurry and then pasting the mixture onto Cu foils (18 μm in thickness). The electrodes were dried at 70 °C for 12 h and then pressed at 10 MPa. The electrode has a thickness from about 40 μm to about 50 μm and loaded at about 1.5 mg–2.0 mg. The CR2016 coin cells were then assembled in an argon-filled glove box using Li metal as the anode, Celgard 2600 as the separator, and 1 M $LiPF_6$ [dissolved in ethylene carbonate (EC) and diethyl carbonate (DEC) with a 1:1 vol. ratio] as the electrolyte. The Si/G electrode's electrochemical performance was evaluated by galvanostatic discharge–charge measurement using a computer-controlled battery tester at a current density of 200, 400, 800 and 1600 mA g^{-1}, respectively, between 0.05 and 1.2 V. For the purpose comparison, pristine Si and Si/RGO electrodes were also prepared and measured under the same conditions.

Table 1
The Si and graphene content in the Si/G and the Si/RGO composites.

Sample	Feeding ratio (wt%)		Calculated ratio (wt %)[a]	
	Si–COOH	G-PIL	Si	Graphene
Si/G 3/1	75.0	25.0	67.3	32.7
Si/G 2/1	66.7	33.3	61.6	38.4
Si/G 1/1	50.0	50.0	44.6	55.4
Si/G 1/2	33.3	66.7	24.7	75.3
Si/RGO 3/2	60 (pristine Si)	40 (GO)	64.6	35.4

[a] Calculated from TGA.

2.5. Characterization

Fourier transform infrared spectroscopy (FTIR) spectra were obtained with a Nicolet Avatar 320 FTIR spectrometer; 32 scans were collected at a spectral resolution of 1 cm^{-1}. The samples for FTIR measurement were prepared by solution deposition on salt plates. The X-ray photoelectron spectroscopy (XPS) measurements were performed with ESCA 2000 (VG Microtech) using a monochromatized Al Kα anode. A DuPont Q100 thermo-gravimetric analyzer (TGA) was utilized to investigate the thermal stability of the membranes; the samples (~10 mg) were heated from ambient temperature to 850 °C under a nitrogen (air) atmosphere at a heating rate of 10 °C min^{-1}. The morphology of the Si nanoparticles and the graphene sheets in the composites were observed using a JEOL JEM-1200CX-II transmission electron microscope (TEM) operated at 120 kV. Scanning electron microscopy (SEM) images were taken with a Hitachi S-4700 microscope using an accelerating voltage of 15 kV. X-ray diffraction (XRD) spectra were recorded on powdered samples using a Rigaku D/max-2500 type X-ray diffraction instrument.

3. Results and discussion

3.1. Characterization of Si–COOH and G-PIL

The complete fabrication of Si/G composite includes two modification processes: (1) the Si nanoparticles modified with 4-aminobenzyl acid through diazonium chemistry to improve the surface negative charge and facilitate dispersion in water (Si–COOH nanoparticles) [Fig. 1a]; and, (2) the graphene nanosheets modified with PIL, as in our previous study, to change the surface charge from negative to positive (G-PIL nanosheets) [30] [Fig. 1b]. Moreover, the polymer structure can provide sufficient empty space surrounding Si nanoparticles after thermal process to accommodate the volume variation of Si nanoparticles during Li alloying and dealloying processes. XPS, TGA and FTIR analysis confirm the existence of benzoyl acid and the PIL on the surface of Si nanoparticles and graphene nanosheets, respectively. The C 1s XPS spectrum of Si–COOH (Fig. 2a) clearly indicates a considerable number of benzoyl acid groups with four components that correspond to carbon atoms in different functional groups, i.e., the Si–C (282.2 eV), aromatic ring (284.5 eV), the C in C–O bonds (286.5 eV) and the carbonyl C (C=O, 288.5 eV) [37]. For G-PIL, the observation of C–N of C 1s at 286.6 eV, N 1s at 401.7 eV and Br 3d at 67.4 eV after modification with PIL confirms the presence of characteristic polymer anions, or cations, in the modified graphene sheets (Fig. 2b and d). The surface concentration of grafted benzoyl acid groups and modified PIL were estimated from the mass loss given by the difference in char yield values between pristine Si nanoparticles/Si–COOH and RGO/G-PIL: (Fig. S1), indicates that Si–COOH and G-PIL contain ~22% and ~26% modified materials, respectively. FTIR spectroscopy (Fig. S3)

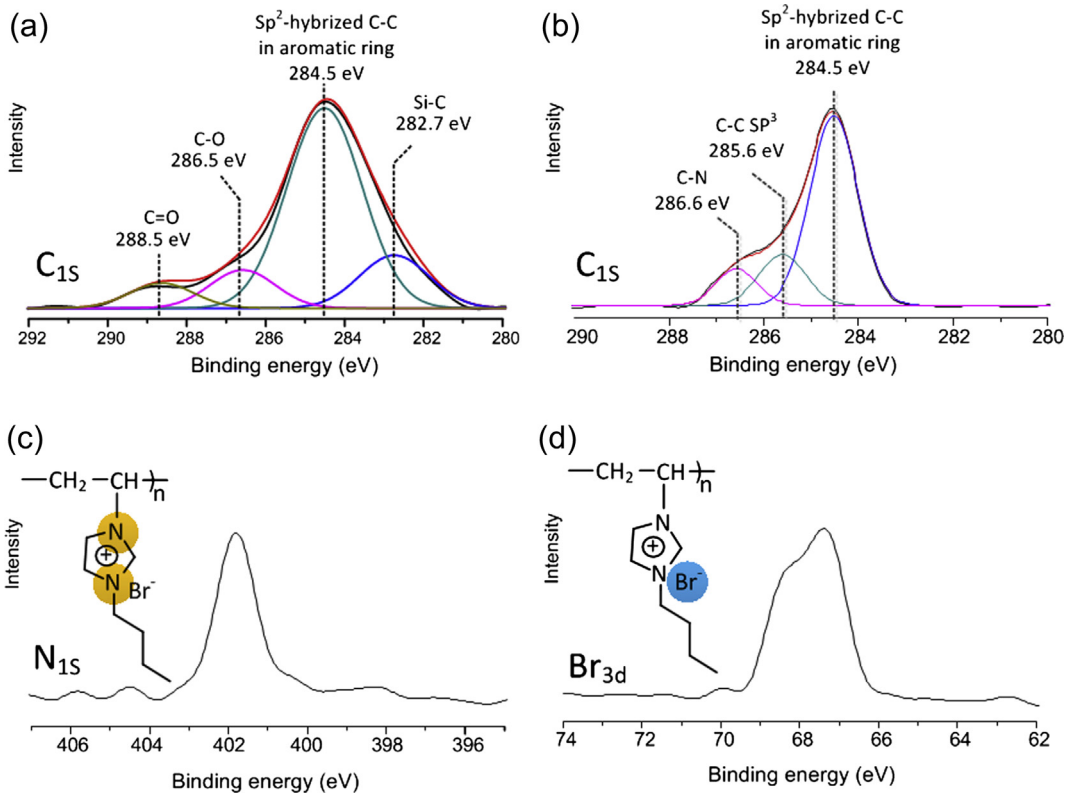

Fig. 2. XPS C 1s spectra of: (a) Si–COOH and (b) G-PIL, (c) XPS N 1s and (d) XPS Br 3d of G-PIL.

gives the characteristic absorption of functional groups and organic molecules on the Si–COOH and G-PIL. After modification with benzoyl acid and ionic polymer, the appearance of new bands, corresponding to the imidazole ring (1187, 1584 cm^{-1}) for G-PIL and the benzoyl acid (1624, 1210 cm^{-1}) for Si–COOH were observed, indicating successful modification and the formation of the corresponding benzoyl acid and PIL modified Si and graphene, respectively.

3.2. Assembly process

To survey the assembly process, we carried out zeta potential measurements. The results show the zeta potentials of Si–COOH nanoparticles and G-PIL are −43 mV and +29 mV, respectively. Si–COOH and G-PIL were separately dispersed in water under sonication with concentrations of 1 mg mL^{-1}. Finally, the Si–COOH/G-PIL composites with different components of Si–COOH and G-PIL (Si–COOH/G-PIL = 3/1, 2/1, 1/1, 1/2; Table 1) were prepared by slowly dispersing aqueous G-PIL into the aqueous Si–COOH to allow the formation, through electrostatic attraction, of a uniform assembly comprising positively charged G-PIL and negatively charged Si–COOH [Fig. 1c]. Fig. 3 shows photographs of aqueous dispersion of the Si–COOH, G-PIL and Si–COOH/G-PIL. Obviously, the Si–COOH and G-PIL sample was stabilized in the water (sample 1 and 6). However, with the addition of G-PIL in aqueous Si–COOH (sample 2), the Si–COOH aqueous became unstable and precipitated immediately. This phenomenon indicated that the G-PIL neutralized the charges on the Si–COOH particles. However, with more G-PIL loading, the remaining Si–COOH was neutralized, while residual graphene-PIL was still stabilized in the water (sample 5). After freeze-drying, the Si–COOH/G-PIL composites were further thermally processed at 500 °C to remove organic materials (including ionic polymer and benzoyl acid groups, as shown in Fig. S1) between Si nanoparticles and graphene nanosheets, to leave empty spaces [Fig. 1d]. It is worth noting that the empty space surrounding each Si nanoparticles allows for the free expansion of Si without mechanical constraint during lithiation.

3.3. Morphological analysis

To verify the morphology, structure and composition of the resulting Si/G composites, we carried out SEM, TEM and XRD analysis. SEM images show that the G-PIL and Si–COOH/G-PIL, without thermal processing, are micrometer-sized composites with rough and wrinkled surfaces. For the Si–COOH/G-PIL composite (Fig. S4), it is easy to see that the Si nanoparticles are well wrapped by graphene sheets to form a bulge-like structure, as indicated with arrows. To examine the result of self-assembly, with respect to the inserted Si nanoparticles in the graphene sheets, the Si/RGO sample, made without electrostatic attraction between Si and graphene, was used as a control. The SEM image (Fig. 4a) shows that Si particles are micrometer-sized aggregates (as

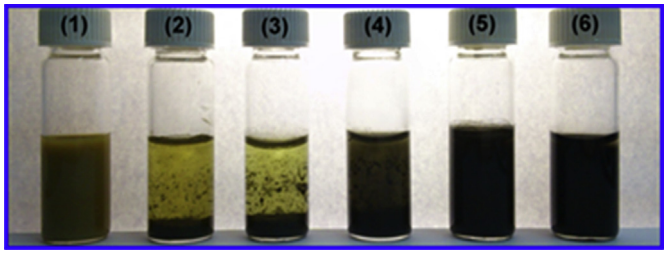

Fig. 3. Photograph of aqueous Si–COOH, G-PIL and Si–COOH/G-PIL. (1) Si–COOH, Si–COOH/G-PIL = (2) 3/1, (3) 2/1, (4) 1/1, (5) 1/2 and (6) G-PIL.

indicated with cycles) in the Si/RGO 3/2 composite after thermal reduction at 500 °C, which may result from high temperature thermal reduction leading to the agglomeration of Si nanoparticles [32]. In contrast, Si nanoparticles are inserted uniformly into graphene layers by self-assembly even after thermal processing. TEM images (Fig. 5) reveal that the micrometer-sized aggregates are made from Si nanoparticles and graphene sheets. The Si nanoparticles were relatively small and distributed more evenly in the Si/G composites than were the Si nanoparticles in the Si/RGO composites. The XRD pattern provides further evidence of the morphology of the Si nanoparticles inserted into graphene layers, see Fig. S5. The characterized peaks of Si [28.5° (111), 47.4° (220) and 56.1° (311)] for all Si/G composites are the same as those of pristine Si nanoparticles, implying that the silicon crystals in the Si/G composites are not destroyed during the thermal process. In the XRD pattern of the G sample obtained by the same procedure for Si/G, the characteristic peak appears at 25.7°, corresponding to a layer-to-layer distance (*d*-spacing) of 0.346 nm, which is close to the *d*-spacing (ca. 0.335 nm) of natural graphite. Inserted Si nanoparticles into graphene layers extended the range of the broad peak to the low-angle position, due to an increase in *d*-spacing between the graphene sheets. Although the interface space can be increased by inserting Si nanoparticles in the graphene sheets, contact between neighboring graphene sheets is unavoidable in the absence of sufficient electrostatic repulsion leading to graphene aggregation during the drying process [31].

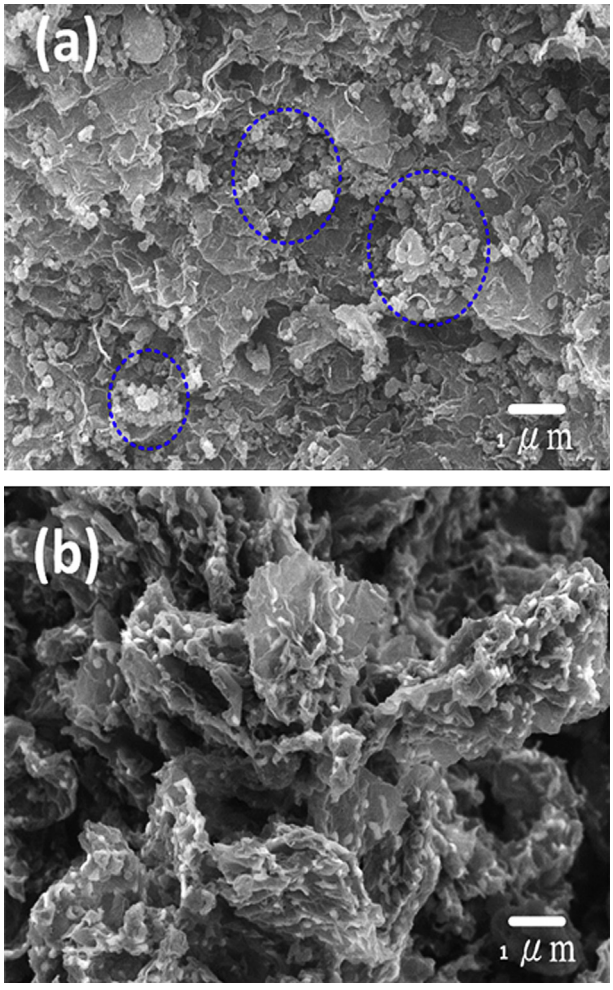

Fig. 4. SEM images of: (a) Si/RGO 3/2 and (b) Si/G 3/1 composites.

3.4. Thermal properties and pore size analysis

The Si content of the Si/G composites can be calculated from Equation (1) and shows that the Si content in the four composites varies from 24.3 wt% to 67.3 wt%, indicating a good correlation between the feeding ratio and calculated ratio. And the control sample Si/RGO 3/2 are calculated to be 64.6 wt%, which was similar to the Si content of Si/G 2/1 composite. In addition, the thermal decomposition temperature of RGO was increased with increasing Si nanoparticles loading, which strongly suggests the thermal stable Si nanoparticles were well dispersed, thereby improving the Si/G composite stability. To understand the specific surface area and pore size distribution of the Si/G composite, Brunauer–Emmett–Teller (BET) N_2 adsorption–desorption analysis was performed. Fig. S6a and S6b show nitrogen isotherm adsorption–desorption curves and the pore size distributions of Si/G 3/1 composite. A BET surface area of 140 $m^2\ g^{-1}$ was measured for the Si/G 3/1 composite which was similar to previous result [39]. The nitrogen adorption–desorption isotherm represents a typical IV-type isotherm with an associated H3 type hysteresis loop, indicating the mesoporous structure of the Si/G composite, which is confirmed by the Barrett–Joyner–Halenda (BJH) pore-size distribution (mesopores of about 3.5–12.1 nm in diameter). These results suggested that the Si/G composites are composed of Si nanoparticles and graphene, where the Si nanoparticles inserted into graphene sheets and the nanospace exists between the Si nanoparticles and graphene sheets. The empty space surrounding each Si nanoparticle is a prerequisite for superior lithium storage because it facilitates the conduction of electrons and the diffusion of lithium ions while providing an elastic buffer to accommodate the volume variation of Si nanoparticles during Li alloying and dealloying processes.

3.5. Electrochemical analysis

The electrochemical performance of the Si/G composite was investigated by cyclic voltammetry (CV) and galvanostatic discharging–charging measurement. Fig. 6a shows typical CV curves of the Si/graphene composite in the potential window of 0.05–1 V at a scan rate of 0.1 mV s^{-1} of the first five cycles. In the first cycle a broad cathodic peak appeared at 0.8 V resulting from the formation of solid electrolyte interphase (SEI), which led to an initial irreversible capacity [38]. The cathodic part of the second cycle displayed two peaks at 0.05 and 0.2 V, which were attributed to the formation of Li–Si alloys. These results are consistent with the data previously reported in the literature for Si/graphene electrodes [39–41].

Fig. 6b displays the discharge–charge voltage profiles of the pristine Si particles, Si/RGO and Si/G composites cycled at a current density of 200 mA g^{-1}, between voltage limits of 0.05–1.2 V *vs.* Li^+/Li. The Si anode exhibits the highest reversible capacity of 2031 mAh g^{-1} and a Coulombic efficiency (CE) of 77%. For all of the three Si/G composites, both the reversible capacity and CE dropped with an increasing graphene content (Fig. 6b and Fig. S7), this may result from an increase in the irreversible reaction between the graphene with its high surface area and the electrolyte. After the first cycle, the CE increased and stabilized at 98%–100% in subsequent cycles. For comparison, bare Si nanoparticles and the Si/RGO 3/2 control sample (containing 64.6 wt% Si) were also tested for lithium-ion batteries. It is noteworthy that the capacity of Si in the Si/RGO 3/2 composite is much higher that of Si in Si/G 3/1 for the first few cycles. The XPS spectrum of Si after chemical and heat treatment (Fig. S8) clearly indicates some changes occurring on the surface after a series of chemical and heat treatments. Silicon oxide growth on the Si surface was confirmed with an increase in the chemical shift component in the Si 2p core-level spectra at around

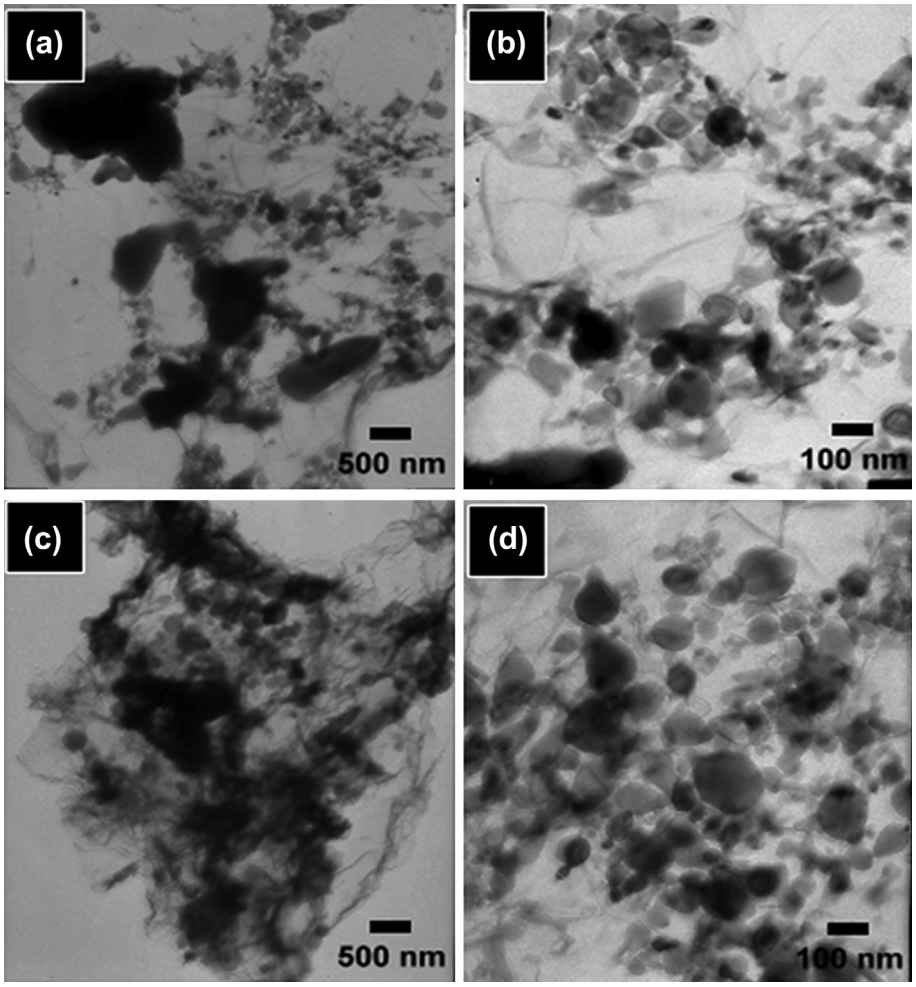

Fig. 5. TEM images of Si/RGO and Si/G composites: (a), (b) Si/RGO = 3/2; (c), (d) Si/G = 3/1.

104.5 eV. Moreover, a signal due to oxygen was observed at 534.7 eV (O 1s) and assigned to adventitiously adsorbed hydrocarbons having oxygen bonded to carbon (285.5 eV) as shown after heat treatment. It is reasonable to assume that these adventitious hydrocarbons could stem from the residual material's benzoyl acid groups, and/or carbonaceous materials present in the laboratory environment. These residual materials and silicon oxide on the Si surface reduced electrical conductivity for the Si/G composites and may potentially adversely affect the performance of Si particles, resulting in the specific capacity of Si in Si/G composites remaining lower than 1600 mAh g^{-1} for the first few cycles.

Under charge/discharge condition, fast capacity fading for anodes made from bare Si nanoparticles was observed and <21% of the initial capacity remained after 40 cycles (Fig. 6c). By introducing graphene nanosheets into nanoparticles without a self-assembled technique (Si/RGO 3/2 composite), the cycling stability showed minimal improvements and more than half of its initial capacity was lost in 40 cycles. All the Si/G composites showed much better cycling performance than the bare Si nanoparticle and Si/RGO 3/2 composite, which had only a slight capacity decay before 40 cycles. Moreover, we note that the Si/G 3/1 composite shows increasing in the initial 12 cycles (Fig. 6c), which is also confirmed by CV measurement (Fig. 6a). This phenomenon may be associated with a special activation process of Si anode. Since the Li–Si alloying/dealloying process results in significant internal structural changes for the Si anode, the reconstruction of crystal structure near the Si surface cause the activation phenomenon [42,43]. For capacity retention properties, no obvious change in charge/discharge profile was found in the Si/G 3/1 composite after 50 cycles (capacity retention: >95%) and <0.25% capacity decreasing per cycle before 150 cycles with the reversible capacity still as high as 803 mAh g^{-1} in the 100th cycle, which is more than 2 times higher than that of the theoretical specific capacity of a traditional graphite anode (LiC_6, 370 mAh g^{-1}) (Fig. 7).

The RGO anode displays a capacity 1258 mAh g^{-1} and 255 mAh g^{-1} for the first charge–discharge cycle respectively with the reversible capacity of only 20.3%. The cell performance of the graphene in the Si/graphene composites are similar as previously reported in literature. The Si contribution from Si/RGO or Si/G composites can be calculated by following Equation and the results was shown in Fig. 6d [33].

$$C_{Si} = [C_C - C_G \times (1 - X_{Si})]/X_{Si}$$

where C_{Si}, C_C and C_G is the specific capacity of calculated pure Si, Si/G composite, and RGO, respectively. X_{Si} is the content of Si in the Si/RGO or Si/G composites (Table 1). It can be seen that the Si/G composites shown great enhancement of the capacity retention as compared with bare Si nanoparticle and Si/RGO 3/2 composite, based on the calculated contribution of the pure Si. This result indicated that well dispersed Si nanoparticles are electrically connected with the graphene so that all the Si nanoparticles will

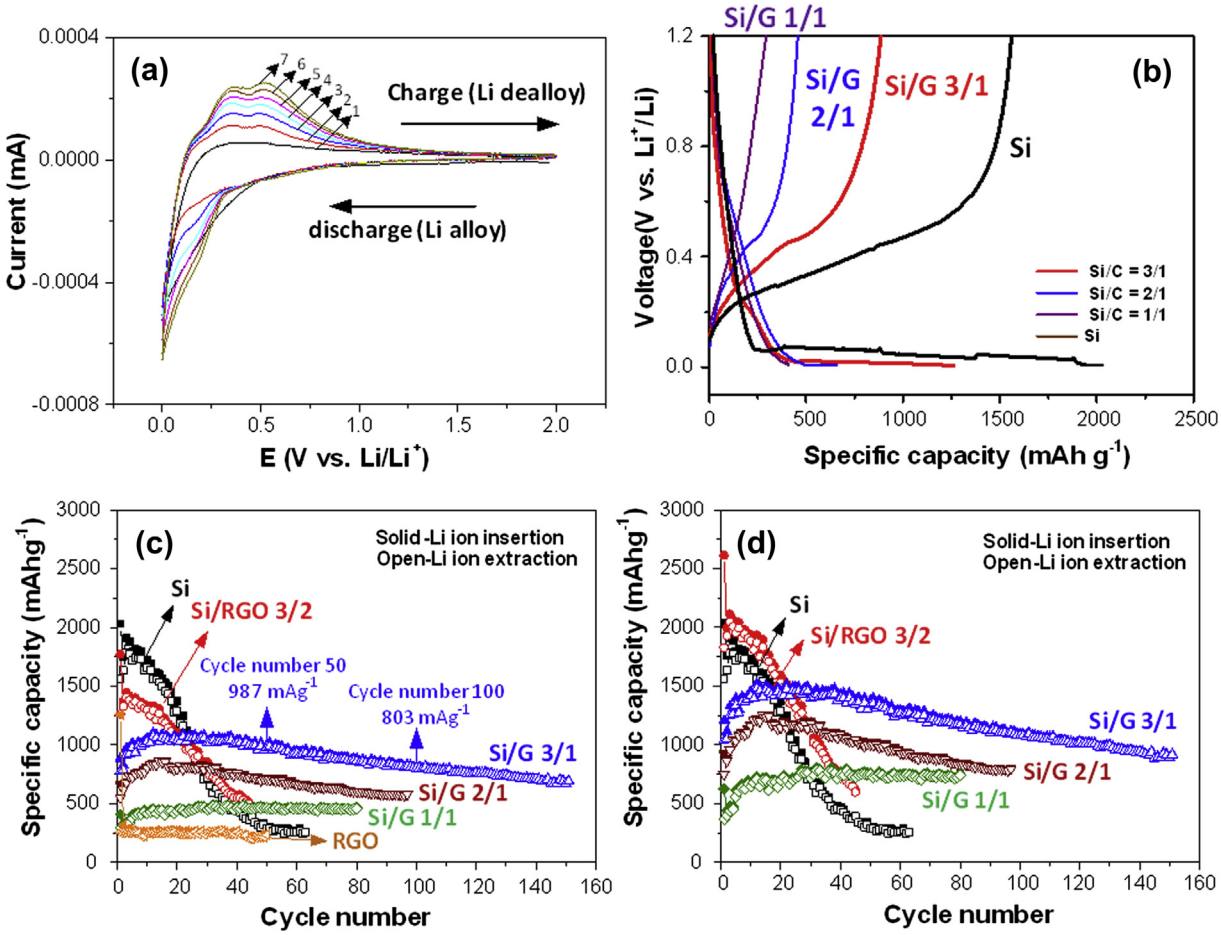

Fig. 6. (a) Cyclic voltammetry profiles of the Si/G 3/1 composites and (b) galvanostatic discharge–charge curves for bare Si nanoparticle and Si/G composites. Cycling performance of Si nanoparticle, RGO, Si/RGO and Si/G composite anodes. The capacity is calculated on the weight of composite (c) and Si (d), respectively. The current density is 200 mA g^{-1}.

contributed to the capacity and the ability of charge transfer can be enhanced [44].

Moreover, Fig. 8 shows a significantly improved property of the Si/G 3/1 composite to be their rate capability. As the current densities increases from 200 to 800 and 1600 mA g^{-1}, the Si/G 3/1 composite displays reversible and stable capacities of 1100, 870, and 735 mAh g^{-1}. Finally, electrochemical impedance spectroscopy (EIS) measurements of the samples, after being used for 40 cycles, clearly indicated enhanced electrical conductivity and reduced SEI formation for the Si/G 3/1 composites compared to the Si/RGO 3/2 composites (Fig. S9). This result indicated that Si/G composite prepared by the self-assembly approach can provide better separation, thus preventing the agglomeration of Si nanoparticles than is the case with a simple mixture of graphene and Si nanoparticles.

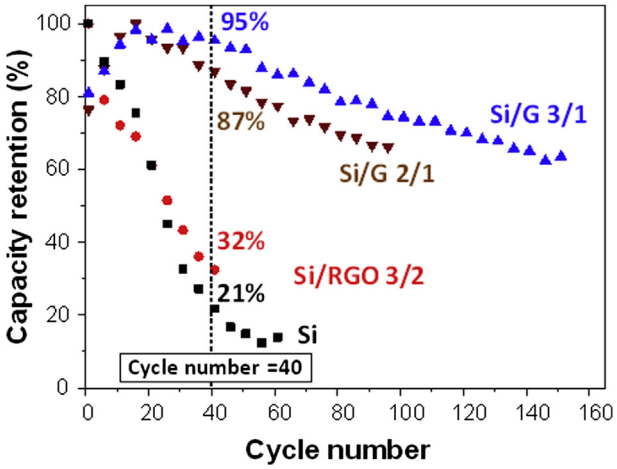

Fig. 7. Capacity retention of the Si nanoparticle, Si/RGO and Si/G composites.

The resulting Si/G (Si/G 3/1) composite delivers a reversible capacity of 987 mAh g^{-1} and 803 mAh g^{-1} in the 50th and 100th cycle, respectively, which is comparable with or better than in previous reports, such as those on Si/RGO composite prepared by thermally reduced mixture simply comprising GO and Si nanoparticles (~750 mAh g^{-1}, 30 cycles) [32], Si/G composite prepared by simply mixing of Si nanoparticles and graphene (~1200 mAh g^{-1}, 30 cycles [33]; 977 mAh g^{-1}, 30 cycles [45]), Si/G composite prepared by covalent binding approach (828 mAh g^{-1}, 50 cycles) [40] and a 3D porous architecture of Si/G composite (1000 mAh g^{-1}, 30 cycles) [46]. The excellent cyclability and rate capability of the Si/G electrodes is believed to originate from the following: (I) the high electrical conductivity and high surface area of graphene sheets facilitating electron transport though the underlying graphene sheets to the Si nanoparticles and the penetration of the electrolyte to the Si nanoparticles, (II) the buffer effect on the volume change (deformation pressure from Li–Si alloy and dealloy process) comes from large amount of void spaces provided by the Si/G composite with nanoporous structure, and (III) most importantly, the self-assembly technique ensures a

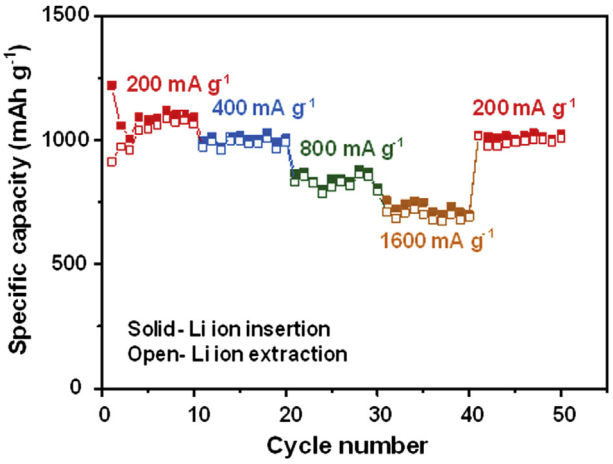

Fig. 8. Rate capability of the Si/G 3/1 composite.

homogeneous dispersion of Si nanoparticles on the graphene sheets and an increased contribution of Si nanoparticles towards capacity. This means Si particle self-aggregation is reduced, thus providing a potential benefit for the stable electrochemical cycling of materials.

4. Conclusions

We have developed a novel method for the preparation of Si nanoparticles intercalated in graphene sheets by combining a self-assembly technique and a thermal process. The presence of non-covalent linkages prevents the aggregation of Si nanoparticles and guarantees that Si nanoparticles are uniformly inserted into graphene layers. The mesoporous structure of the Si/G composite allows for the free expansion and contraction of Si nanoparticles during lithiation and delithiation without mechanical constraint or tension being imposed. Combining these advantages in Si/G composites, the resulting composites exhibit both a remarkably improved cycling performance and rate performance in comparison with bare Si nanoparticles and Si/RGO. At a current density of 200 mA g^{-1}, the Si/G electrodes delivered a capacity of 803 mAh g^{-1} in 100 cycles and <0.25% capacity decreasing per cycle before 150 cycles. The electrode still exhibited a reversible capacity of 748 mAh g^{-1} in the 40th cycle at a rate of 1600 mA g^{-1}. We believed this technique can be applied to other carbon conductive additives together with Si or other nanosized active compounds.

Appendix A. Supplementary data

Supplementary data related to this article can be found at http://dx.doi.org/10.1016/j.jpowsour.2013.08.048.

References

[1] U. Kasavajjula, C. Wang, A.J. Appleby, J. Power Sources 163 (2) (2007) 1003–1039.
[2] J.M. Tarascon, M. Armand, Nature 414 (6861) (2001) 359–367.
[3] H.K. Liu, Z.P. Guo, J.Z. Wang, K. Konstantinov, J. Mater. Chem. 20 (45) (2010) 10055–10057.
[4] H. Ma, F. Cheng, J.Y. Chen, J.Z. Zhao, C.S. Li, Z.L. Tao, et al., Adv. Mater. 19 (22) (2007) 4067–4070.
[5] C. Martin, M. Alias, F. Christien, O. Crosnier, D. Bélanger, T. Brousse, Adv. Mater. 21 (46) (2009) 4735–4741.
[6] A. Magasinski, P. Dixon, B. Hertzberg, A. Kvit, J. Ayala, G. Yushin, Nat. Mater. 9 (4) (2010) 353–358.
[7] Y. Oumellal, N. Delpuech, D. Mazouzi, N. Dupre, J. Gaubicher, P. Moreau, et al., J. Mater. Chem. 21 (17) (2011) 6201–6208.
[8] Y. Yu, L. Gu, C. Zhu, S. Tsukimoto, P.A. van Aken, J. Maier, Adv. Mater. 22 (20) (2010) 2247–2250.
[9] M. Yoshio, T. Tsumura, N. Dimov, J. Power Sources 146 (1–2) (2005) 10–14.
[10] H. Kim, M. Seo, M.-H. Park, J. Cho, Angew. Chem. Int. Ed. 49 (12) (2010) 2146–2149.
[11] Y.-S. Hu, R. Demir-Cakan, M.-M. Titirici, J.-O. Müller, R. Schlögl, M. Antonietti, et al., Angew. Chem. Int. Ed. 47 (9) (2008) 1645–1649.
[12] S.-H. Ng, J. Wang, D. Wexler, K. Konstantinov, Z.-P. Guo, H.-K. Liu, Angew. Chem. Int. Ed. 45 (41) (2006) 6896–6899.
[13] J. Guo, C. Wang, Chem. Commun. 46 (9) (2010) 1428–1430.
[14] J.S. Bridel, T. Azaïs, M. Morcrette, J.M. Tarascon, D. Larcher, Chem. Mater. 22 (3) (2009) 1229–1241.
[15] Z. Wen, D. Lu, J. Lei, Y. Fu, L. Wang, J. Sun, J. Electrochem. Soc. 158 (7) (2011) A809–A813.
[16] C. Martin, O. Crosnier, R. Retoux, D. Bélanger, D.M. Schleich, T. Brousse, Adv. Funct. Mater. 21 (18) (2011) 3524–3530.
[17] P. Gao, Y. Nuli, Y.-S. He, J. Wang, A.I. Minett, J. Yang, et al., Chem. Commun. 46 (48) (2010) 9149–9151.
[18] J.L. Gomez-Camer, J. Morales, L. Sanchez, J. Mater. Chem. 21 (3) (2011) 811–818.
[19] P.-C. Chen, J. Xu, H. Chen, C. Zhou, Nano Res. 4 (3) (2011) 290–296.
[20] W. Zhou, S. Upreti, M.S. Whittingham, Electrochem. Commun. 13 (2) (2011) 158–161.
[21] S. Stankovich, D.A. Dikin, G.H.B. Dommett, K.M. Kohlhaas, E.J. Zimney, E.A. Stach, et al., Nature 442 (7100) (2006) 282–286.
[22] D.A. Dikin, S. Stankovich, E.J. Zimney, R.D. Piner, G.H.B. Dommett, G. Evmenenko, et al., Nature 448 (7152) (2007) 457–460.
[23] T. Ramanathan, A.A. Abdala, S. Stankovich, D.A. Dikin, M. Herrera Alonso, R.D. Piner, et al., Nat. Nanotechnol. 3 (6) (2008) 327–331.
[24] M. Liang, L. Zhi, J. Mater. Chem. 19 (33) (2009) 5871–5878.
[25] M.D. Stoller, S. Park, Y. Zhu, J. An, R.S. Ruoff, Nano Lett. 8 (10) (2008) 3498–3502.
[26] F. Schedin, A.K. Geim, S.V. Morozov, E.W. Hill, P. Blake, M.I. Katsnelson, et al., Nat. Mater. 6 (9) (2007) 652–655.
[27] J.D. Fowler, M.J. Allen, V.C. Tung, Y. Yang, R.B. Kaner, B.H. Weiller, ACS Nano 3 (2) (2009) 301–306.
[28] H.A. Becerril, J. Mao, Z. Liu, R.M. Stoltenberg, Z. Bao, Y. Chen, ACS Nano 2 (3) (2008) 463–470.
[29] C.-Y. Tseng, Y.-S. Ye, M.-Y. Cheng, K.-Y. Kao, W.-C. Shen, J. Rick, et al., Adv. Energy Mater. 1 (6) (2011) 1220–1224.
[30] Y.-S. Ye, C.-Y. Tseng, W.-C. Shen, J.-S. Wang, K.-J. Chen, M.-Y. Cheng, et al., J. Mater. Chem. 21 (28) (2011) 10448–10453.
[31] Y.-S. Ye, Y.-N. Chen, J.-S. Wang, J. Rick, Y.-J. Huang, F.-C. Chang, et al., Chem. Mater. 24 (15) (2012) 2987–2997.
[32] H. Xiang, K. Zhang, G. Ji, J.Y. Lee, C. Zou, X. Chen, et al., Carbon 49 (5) (2011) 1787–1796.
[33] S.-L. Chou, J.-Z. Wang, M. Choucair, H.-K. Liu, J.A. Stride, S.-X. Dou, Electrochem. Commun. 12 (2) (2010) 303–306.
[34] J.K. Lee, K.B. Smith, C.M. Hayner, H.H. Kung, Chem. Commun. 46 (12) (2010) 2025–2027.
[35] X. Zhao, C.M. Hayner, M.C. Kung, H.H. Kung, Adv. Energy Mater. 1 (6) (2011) 1079–1084.
[36] Y.-S. Ye, Y.-J. Huang, C.-C. Cheng, F.-C. Chang, Chem. Commun. 46 (40) (2010) 7554–7556.
[37] C.W. Chen, C.C. Huang, Y.Y. Lin, L.C. Chen, K.H. Chen, Diamond Relat. Mater. 14 (3–7) (2005) 1126–1130.
[38] P. Liu, H. Wu, J. Power Sources 56 (1) (1995) 81–85.
[39] X. Zhou, Y.-X. Yin, L.-J. Wan, Y.-G. Guo, Adv. Energy Mater. 2 (9) (2012) 1086–1090.
[40] S. Yang, G. Li, Q. Zhu, Q. Pan, J. Mater. Chem. 22 (8) (2012) 3420–3425.
[41] X. Zhou, Y.-X. Yin, L.-J. Wan, Y.-G. Guo, Chem. Commun. 48 (16) (2012) 2198–2200.
[42] H.-C. Shin, J.A. Corno, J.L. Gole, M. Liu, J. Power Sources 139 (1–2) (2005) 314–320.
[43] P. Gao, J. Fu, J. Yang, R. Lv, J. Wang, Y. Nuli, et al., Phys. Chem. Chem. Phys. 11 (47) (2009) 11101–11105.
[44] S.-M. Paek, E. Yoo, I. Honma, Nano Lett. 9 (1) (2008) 72–75.
[45] H.-C. Tao, L.-Z. Fan, Y. Mei, X. Qu, Electrochem. Commun. 13 (12) (2011) 1332–1335.
[46] X. Xin, X. Zhou, F. Wang, X. Yao, X. Xu, Y. Zhu, et al., J. Mater. Chem. 22 (16) (2012) 7724–7730.